ACS APPLIED MATERIALS & INTERFACES

Research Article

www.acsami.org

All-Solid-State Flexible Supercapacitors Based on Highly Dispersed Polypyrrole Nanowire and Reduced Graphene Oxide Composites

Chenfei Yu, Peipei Ma, Xi Zhou, Anqi Wang, Tao Qian, Shishan Wu,* and Qiang Chen*

School of Chemistry and Chemical Engineering, Nanjing University, Nanjing 210093, P. R. China

Supporting Information

ABSTRACT: Highly dispersed polypyrrole nanowires are decorated on reduced graphene oxide sheets using a facile in situ synthesis route. The prepared composites exhibit high dispersibility, large effective surface area, and high electric conductivity. All-solid-state flexible supercapacitors are assembled based on the prepared composites, which show excellent electrochemical performances with a specific capacitance of 434.7 F g^{-1} at a current density of 1 A g^{-1}. The as-fabricated supercapacitor also exhibits excellent cycling stability (88.1% capacitance retention after 5000 cycles) and exceptional mechanical flexibility. In addition, outstanding power and energy densities were obtained, demonstrating the significant potential of prepared material for flexible and portable energy storage devices.

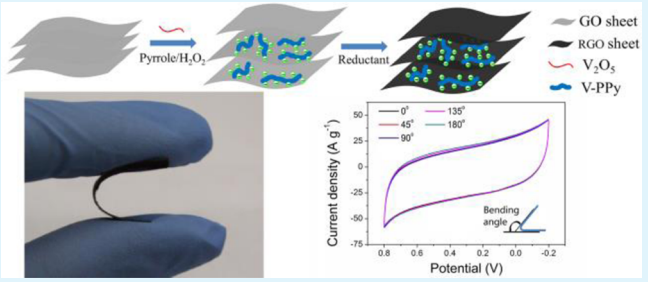

KEYWORDS: *energy storage, supercapacitors, flexible, polypyrrole nanowire, reduced graphene oxide, highly dispersed*

INTRODUCTION

Supercapacitors have attracted a lot of attention as one kind of novel energy storage device, due to their higher power density than batteries, longer cycling stability, and higher energy density than traditional capacitors.[1−4] Therefore, supercapacitors have shown great potential in portable electronics.[5,6] Different from traditional supercapacitors, all-solid-state flexible supercapacitors use polymer gel as electrolyte. With the application of polymer gel electrolytes, the all-solid-state supercapacitors are expected to become flexible, wearable, and environmentally friendly energy storage devices.[7−9] In order to achieve better electrochemical performance, finding appropriate electroactive materials is a promising strategy toward appropriate all-solid-state supercapacitors. Until now, many kinds of nanostructured electrodes have been developed, including graphene,[10−12] metal oxides,[13−15] and conductive polymers,[16,17] etc.

Graphene, one kind of novel carbon material, has shown great potential in supercapacitor devices. Graphene obtains high electronic conductivity, excellent mechanical flexibility, high specific surface area, and chemical stability.[18,19] Reduced graphene oxide (RGO) could be categorized as chemically derived graphene, which is similar to graphene in a number of aspects.[20] However, with the reduction of graphene oxide (GO), oxygen-containing groups largely decrease, which shows that the electrostatic repulsions are too weak to counteract strong $\pi-\pi$ interaction between RGO sheets. The agglomeration appears among RGO sheets, which lead to the lower surface area and slower electron transport rate and therefore unsatisfactory capacitive performance.[21] Hence, various nanostructured functional materials (e.g., metal oxides,[22−24] carbon nanotubes,[25,26] and conducting polymers[27−29]) have been hybridized with RGO to improve capacitive performance.

Polypyrrole (PPy), a kind of the most important conducting polymers, is treated as one of the potential materials for supercapacitors among pseudocapacitance materials. PPy has good environmental stability, low cost synthesis, good conductivity, unusual doping/dedoping chemistry, and high redox pseudocapacitive charge storage.[30,31] PPy nanowires show many outstanding characteristics, such as the optimum of the ion-diffusion pathway, higher energy storage pseudocapacitance, and higher surface area than bulk PPy material, which lead to the improvement of its capacitance over that of bulk PPy material.[32] In this work, we design an all-solid-state supercapacitor based on novel PPy nanowires and reduced graphene oxide (V-PPy/RGO) composites. The PPy nanowires (V-PPy), which obtain high dispersibility, are facilely synthesized in the presence of V_2O_5 seed and H_2O_2. Meanwhile, the V-PPy could be decorated on the surface of GO via $\pi-\pi$ interaction. Then, the nanocomposites are reduced by hydrazine (Figure 1). The decorative V-PPy could prevent the aggregation of RGO sheets owing to electrostatic repulsions. Hence, high dispersibility has appeared. Furthermore, when the nanocomposite material has both layered and tubular structure, not only the diffusion of ions and electron transport will be improved but also its cycling stability and capacitance are superior to traditional material.[33]

Received: July 16, 2014
Accepted: September 23, 2014
Published: September 23, 2014

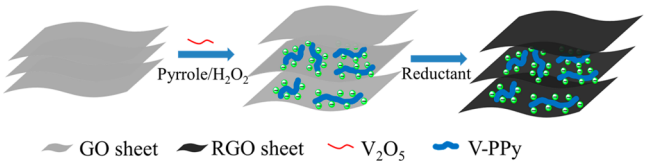

Figure 1. Scheme showing the synthetic route of V-PPy/RGO composites.

RESULTS AND DISCUSSION

The morphology and structure of V-PPy and the V-PPy/RGO composites were characterized using transmission electron microscopy (TEM) and scanning electron microscopy (SEM) (Figure 2 and Figure S1 and Figure S2, Supporting Information). The weight feed ratio of V-PPy to RGO was varied as 2:1, 1:1, and 1:2, and the resulting composites were named as V-PPy/RGO21, V-PPy/RGO11, and V-PPy/RGO12, respectively. Figure 2A and 2B show uniform nanowire morphology of V-PPy with diameters around 80 nm. As shown in Figure 2C and 2D, V-PPy nanowires are completely coated on RGO sheets. Figure 2E and F are high-resolution transmission electron microscopy (HRTEM) images, which showed the partial morphology of a composite. The morphology of the RGO sheet shows a wrinkle and crumple-like surface, with a thickness of about 2.86 nm. More details are presented by Figure S1 and Figure S2 (Supporting Information). For V-PPy/RGO21, the overabundance of V-PPy nanowires cannot be completely adsorbed on the surface of RGO sheets. As to V-PPy/RGO12, the amount of V-PPy nanowires decreases, and the RGO nanosheets can be seen clearly.

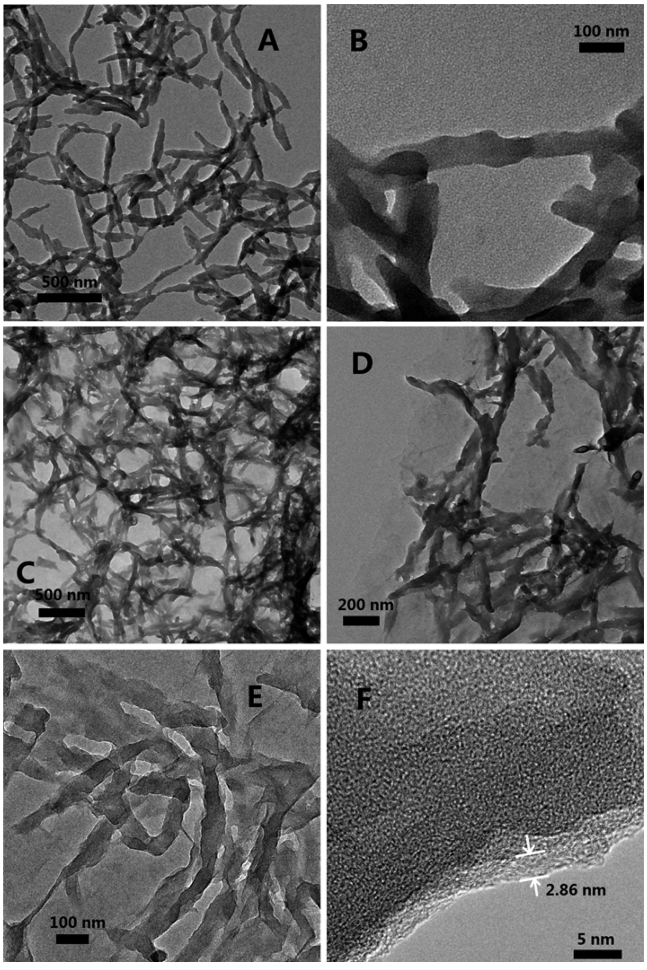

Figure 2. TEM images of (A) V-PPy nanowire and (B) V-PPy nanowire with partial enlargement. TEM images of (C) V-PPy/RGO11 and (D) V-PPy/RGO11 with partial enlargement. HRTEM images of (E) V-PPy/RGO11 and (F) V-PPy/RGO11 with partial enlargement.

Figure 3 shows the photograph of RGO, V-PPy, and V-PPy/RGO composite dispersions. All of the dispersions were placed for 72 h after ultrasonication to reveal the dispersibility directly. As shown in Figure 3, the V-PPy dispersion is stable without significant precipitation, while the RGO sheets aggregate and precipitate in aqueous solvent. However, the V-PPy/RGO dispersion can be well-stable without the observation of any floating or precipitate particles. The excellent dispersibility of the V-PPy/RGO in our present study can be attributed to the electrostatic repulsions between the coated V-PPy nanowires. When V-PPy nanowires were decorated on RGO sheets, it could prevent the aggregation of RGO. The data of zeta potentials are presented in Table 1, and the result is according with that of the above, which further confirms the improvement of electrostatic repulsions between the prepared sheets.

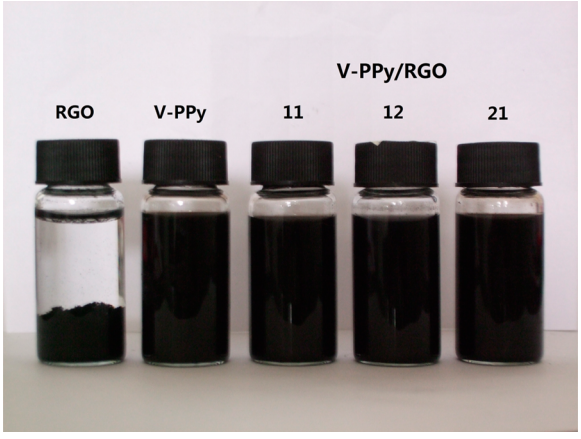

Figure 3. Photographs of RGO, V-PPy, and V-PPy/RGO composites dispersed in water (1 mg/mL) after 1 h ultrasonication and stood for 72 h.

The structure of the V-PPy, RGO, and V-PPy/RGO was studied by Raman spectra (Figure 4A). The peaks of PPy were located at 977, 1050, 1338, and 1578 cm^{-1}. The small peaks near 977 and 1050 cm^{-1} have been associated with the bipolaronic structure and C−H in-plane deformation of V-PPy. The C═C backbone stretching and ring-stretching mode of the V-PPy lead to the peaks near 1578 and 1338 cm^{-1}, respectively.[34,35] Raman spectra of the RGO-based nanocomposite have very distinctive peaks for the D and G bands, which are located at about 1350 and 1584 cm^{-1}, respectively. The changes of D/G intensity ratio can demonstrate the variable ratio of C_{sp3}/C_{sp2}. When the V-PPy/RGO ratio increases, the D/G intensity ratio gets close to the D/G ratio of V-PPy. Meanwhile, the characteristic peak for PPy at 977 and 1050 cm^{-1} disappears when the V-PPy/RGO ratio decreases. Both of these variations confirm the successful fabrication of V-PPy/RGO composites.

Table 1. Zeta Potential Data of RGO, V-PPy, and V-PPy/RGO Composites

	RGO	V-PPy	V-PPy/RGO11	V-PPy/RGO12	V-PPy/RGO21
zeta potential (mV), pH = 7.0	−3.5	−38.5	−37.9	−37.7	−38.2

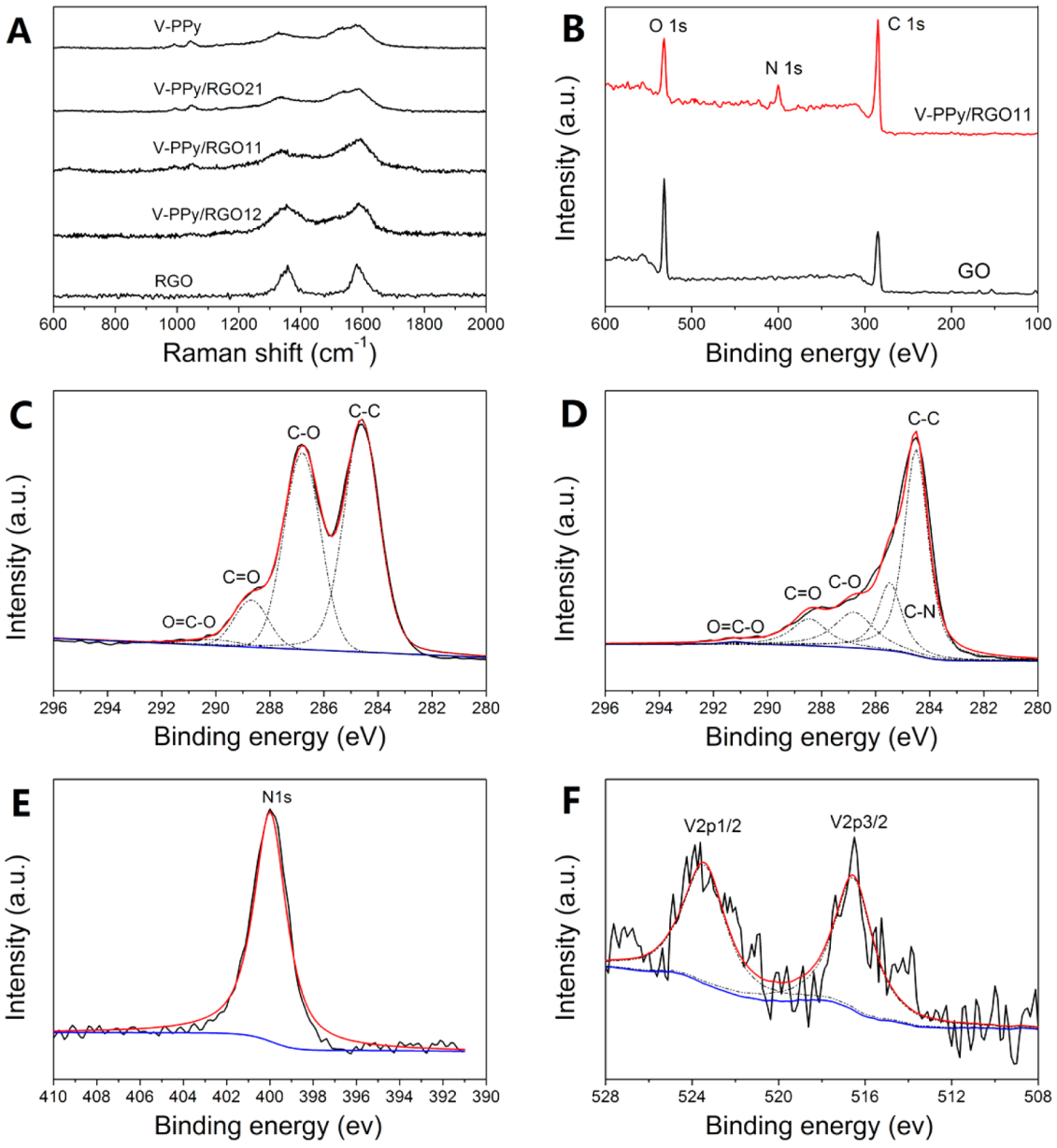

Figure 4. (A) Raman spectra of pure V-PPy, RGO, and V-PPy/RGO and (B) XPS spectra of the pristine GO and prepared V-PPy/RGO11 composite. High-resolution XPS spectra of (C) C 1s of pristine GO, (D) C 1s, (E) N 1s, and (F) V 2p of V-PPy/RGO11.

X-ray photoelectron spectroscopy (XPS) was used to study the structure of the V-PPy/RGO composite. Through analysis of wide region spectroscopy (Figure 4B) of GO and the V-PPy/RGO11 composite from XPS study, it could be observed that for GO sheets the C/O intensity ratio was 0.57, and that for V-PPy/RGO11 is 1.86, which is mainly due to the addition of V-PPy. Most of the oxygen functionality has been successfully removed after reduction. In addition, a new peak of N 1s appears in the spectra of V-PPy/RGO11, corroborating the successful fabrication of V-PPy. The high-resolution XPS spectrum of the C 1s region of GO is shown in Figure 4C, which can be disintegrated into four peaks. The four peaks are located at C−C (284.5 eV), C−O (286.8 eV), C═O (288.7 eV), and O═C−O (291.0 eV).[36] The peak intensity of C−O is comparable to the intensity of C−C, and the C═O peak is also very high. Figure 4D shows the C 1s region of V-PPy/RGO11. The peak intensity of C−O and C═O decreases, as a result of the in situ polymerization of V-PPy and the reduction of GO, while the C−C peak becomes prominent. Besides the changes of C−O and C═O, a new carbon bond of C−N with the binding energy of 285.4 eV appears, due to N atoms in the pentagonal ring of pyrrole for V-PPy/RGO. From Figure 4E, it can be seen that the only peak at 400.0 eV corresponds to N 1s, demonstrating the decoration of V-PPy in composite. The high-resolution XPS spectrum of V could be deconvoluted into two peaks (Figure 4F). The peaks with binding energy of 516.7 and

dx.doi.org/10.1021/am5059603 | ACS Appl. Mater. Interfaces 2014, 6, 17937−17943

523.7 eV are associated with V 2p3/2 and 2p1/2, respectively.[37] Table S1 (Supporting Information) records the elemental composition of V-PPy/RGO composites determined from XPS. As the V-PPy ratio increases, the V content and N content also increase.

UV−vis spectra could be used to analyze the interaction between GO sheets and the V-PPy nanowire. The UV spectra of V-PPy, GO, and V-PPy/GO11 are shown in Figure S3 (Supporting Information). The predominant absorption peak of GO at 228 nm is associated with the $\pi-\pi$ transition of aromatic C=C bonds.[38] With the addition of V-PPy, the predominant peak at 228 nm for GO shifts to 238 nm for V-PPy/GO11, which may be attributed to the $\pi-\pi$ interaction between the polymer backbone and the GO sheets.

To estimate the effective surface area of the V-PPy/RGO composites, cyclic voltammetry (CV) tests were employed for analysis in the solution of 10 mM $K_3Fe(CN)_6$ and 0.1 M KCl (Figure S4A, Supporting Information). The calculations of effective surface area come from the Randles−Sevcik equation

$$i_p = (2.687 \times 10^5) n^{3/2} v^{1/2} D^{1/2} AC \quad (1)$$

where i_p refers to the peak current; n is the number of electrons participating (n = 1, in 10 mM $K_3Fe(CN)_6$); v is the scan rate; D is the diffusion coefficient ($D = 5.7 \times 10^{-6}$ cm^2 s^{-1}, in 0.1 M KCl); A is the surface area, and C is the concentration of $K_3Fe(CN)_6$.[39] As shown in Figure S4B (Supporting Information), the relation was linear between peak current i_p and the square root of scan rate v. For the bare glassy carbon electrode (GCE), RGO, and V-PPy/RGO11 electrodes, the slopes were 0.430, 0.674, and 1.901, respectively. A was calculated to be 0.067 cm^2 (bare GCE), 0.105 cm^2 (RGO), and 0.296 cm^2 (V-PPy/RGO11), indicating that the electrode effective surface area was increased obviously after the modification of such unique hybrids, which would enhance the electrochemical properties.

An all-solid-state symmetric flexible supercapacitor was assembled with two V-PPy/RGO electrodes based on PET substrate with nickel-plated conductive fabric using solid PVA-H_2SO_4 electrolyte and separator (Figure 5). CV and

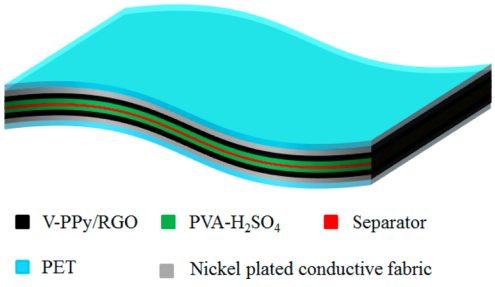

Figure 5. Schematic diagram of the all-solid-state device with PVA-H_2SO_4 polymer gel as electrolyte.

galvanostatic charge/discharge tests were used to evaluate the electrochemical performance of those prepared supercapacitors. CVs of the V-PPy/RGO11 supercapacitor with a voltage window of −0.2−0.8 V are shown in Figure 6A. The CVs at different scan rates from 30 to 300 mV/s exhibit rectangular and symmetric shape, demonstrating the ideal capacitive characteristic of V-PPy/RGO11. As shown in Figure 6B, galvanostatic charge/discharge curves of the prepared V-PPy/RGO11 between −0.2 and 0.8 V were obtained at different current densities in the range of 1−20 A g^{-1}. The galvanostatic charge/discharge curves are linear and symmetric, indicating the good capacitive behavior. Figure 6C shows the detailed specific capacitance of V-PPy, RGO, and V-PPy/RGO supercapacitors at different current densities. The highest specific capacitance of V-PPy/RGO11 could be determined to be 434.7 F g^{-1} at a current density of 1 A g^{-1}, almost quadruple that of RGO (117.2 F g^{-1}). Even as the current density increases to 20 A g^{-1}, the specific capacitance of V-PPy/RGO11 also retains a high value of 361.1 F g^{-1}, 83% retention of the capacitance at 1 A g^{-1}, which probably results from the high dispersibility, the increasing effective surface area, and the combination of tubular and layered structures, accessible for fast ion transportation.

The galvanostatic charge/discharge curves of V-PPy, RGO sheets, and V-PPy/RGO supercapacitor devices with a voltage window of −0.2−0.8 V at a current density of 1 A g^{-1} were shown in Figure S5 (Supporting Information), respectively. The electrical conductivity of V-PPy, RGO, and V-PPy/RGO composites was shown in Table S2 (Supporting Information). The electrical conductivity of V-PPy is poor, indicating that the excess V-PPy nanowires of V-PPy/RGO21 lead to the lower specific capacitance than V-PPy/RGO11. In the V-PPy/RGO12 composite, the less V-PPy nanowires cannot completely prevent RGO restack, which may reduce the specific capacitance compared to V-PPy/RGO11.

The Ragone plot, consisting of energy density and power density, is an important parameter for the energy storage device. Figure 6D shows the Ragone plot of the V-PPy/RGO11 all-solid-state supercapacitor device. The solid-state supercapacitor shows a high energy density of 60.37 Wh kg^{-1} at a power density of 0.5 kW kg^{-1}. Moreover, upon increasing the power density up to 10 kW kg^{-1}, the energy density of V-PPy/RGO11 remains at 50.14 Wh kg^{-1}. Such a high and stable energy density indicates that V-PPy/RGO11 can act as a promising material for practical application in supercapacitors.

This all-solid-state flexible supercapacitor also shows exceptional mechanical flexibility. Figure 7A demonstrates the excellent flexibility and good mechanical properties of the thin film electrodes. Figure 7B shows the similar electrochemical performances under different bending angles. In order to estimate the reliability after continuous bending, the flexible V-PPy/RGO11 supercapacitor was tested after 200 bending cycles of 180° bending angle (Figure S6, Supporting Information). The CV curve after 200 bending cycles is similar to the initial curve, which demonstrates outstanding mechanical robustness.

To demonstrate the practical potential of the V-PPy/RGO11 all-solid-state flexible supercapacitors, we fabricated a tandem supercapacitor device consisting of two pieces of all-solid-state flexible supercapacitors in series. As shown in Figure 7C, a red light-emitting-diode (LED, the lowest working potential is about 1.5 V) could be powered by this tandem supercapacitor device, demonstrating the practical potential application of the V-PPy/RGO11 supercapacitor.

Cycling stability is an important characteristic of supercapacitor, and the cycling life of the V-PPy/RGO11 all-solid-state supercapacitor was tested by galvanostatic charge/discharge technique for 5000 cycles at the current density of 10 A g^{-1}. The V-PPy/RGO11 supercapacitor device shows a slight decrease and remains about 88.1% retention of the initial capacitance after 5000 cycles (Figure 7D), comparable to and even better than those reported for solid-state supercapacitor,

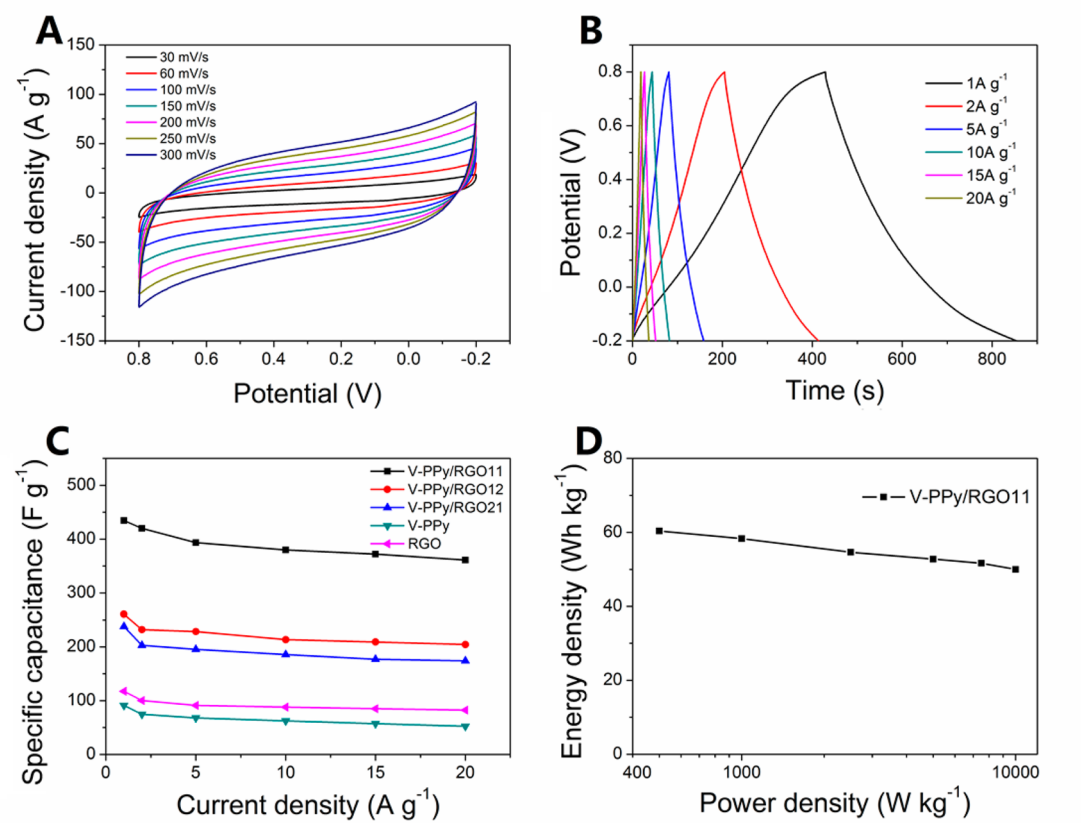

Figure 6. (A) CVs of V-PPy/RGO11 supercapacitor with a voltage window of −0.2−0.8 V at different scan rates. (B) Galvanostatic charge/discharge curves of V-PPy/RGO11 supercapacitor between −0.2 and 0.8 V with different current densities. (C) The specific capacitances of V-PPy, RGO, and V-PPy/RGO composite supercapacitor devices at different current densities. (D) Ragone plots of V-PPy/RGO11.

such as 89% of PANI−GNR−CNT after 1000 cycles,[9] 90.6% of PPy nanofiber/graphene film after 1000 cycles,[40] and 83.6% of polypyrrole electrodes after 2000 cycles.[41] The good electrochemical performance in the cycling test illustrates the outstanding cycling stability of V-PPy/RGO11.

CONCLUSIONS

In summary, V-PPy/RGO composites have been facilely synthetised in the presence of V_2O_5 seed and H_2O_2. The decorative V-PPy could prevent the aggregation of RGO sheets, which has been proved by dispersion photographs and zeta potential data. Raman and XPS measurements demonstrate the successful fabrication of V-PPy/RGO composites. Furthermore, we have successfully fabricated all-solid-state flexible supercapacitors with the V-PPy/RGO composites to achieve excellent capacitive characteristics, superior cycling stability, and outstanding mechanical flexibility, owing to the significant advantage of the decorative V-PPy. We believe the hybrid supercapacitor could be a promising flexible and wearable energy storage system for fast and efficient energy storage in the future.

EXPERIMENTAL SECTION

Synthesis of V-PPy Nanowires. The procedures are as follows: 0.2 mL of pyrrole was first dispersed in 100.0 mL of deionized water under vigorous stirring. An amount of 0.005 g of V_2O_5 seed[42] dispersed in 2 mL of H_2O was dropped in the mixture. In order to initiate polymerization, 5 mL of H_2O_2 was added dropwise to the dispersion. After continuous stirring for 12 h, the color of the dispersion turned to dark, and V-PPy nanowires were obtained. For purification, the obtained dispersion was repeatedly filtered to remove the unreacted reactants and washed with water several times. The powder was then dried under vacuum to yield ∼100 mg of V-PPy nanowires.

Synthesis of V-PPy/RGO. GO was synthesized using a modified Hummer's method[43] and dispersed in water with a concentration of 1.0 mg/1.0 mL of H_2O by ultrasonication. V-PPy/RGO composites were synthesized by using in situ polymerization. Pyrrole was polymerized on the surface of GO by a facile route. Here we take the V-PPy/RGO11 composite as an example, and 0.2 mL of pyrrole and 0.005 g of V_2O_5 were added into 100 mL of GO dispersion under vigorous stirring. When 5 mL of H_2O_2 was dropped in the mixture, in situ polymerization was initiated and lasted for 12 h. The resulting V-PPy/GO11 was then reduced by 0.40 mL of hydrazine hydrate at 90 °C for 6 h. V-PPy/RGO11 composites were obtained, yielding ∼200 mg.

Fabrication of Flexible Solid-State Supercapacitors. PVA/H_2SO_4 gel electrolyte was prepared by adding 6 g of PVA powder and 6 g of H_2SO_4 into 60 mL of deionized water. The mixture was heated at 85 °C under stirring until the solution became clear. The as-prepared V-PPy/RGO was coated on the PET substrate with nickel-plated conductive fabric. Two pieces of freestanding electrodes and a filter paper as separator were immersed into the PVA/H_2SO_4 gel electrolyte and then dried at room temperature for 6 h. Finally, they were assembled into a flexible all-solid-state supercapacitor and evaporated excess water.

Apparatus. TEM images were performed on a JEM 2100 high-resolution TEM. SEM imaging was obtained with a JEOL-JSM-7600F SEM. HRTEM images were performed on a FEI Tecnai F30 operated at 200 kV. Zeta potential was recorded on a Malvern Nano-Z Instrument. Raman analysis was obtained with a Jobin Yvon HR800. XPS spectra were obtained with a PHI 5000 VersaProbe. UV−vis spectra were performed on a Lambda 35 UV−vis spectrometer. The electrical conductivity was determined using the Keithley 2400 source

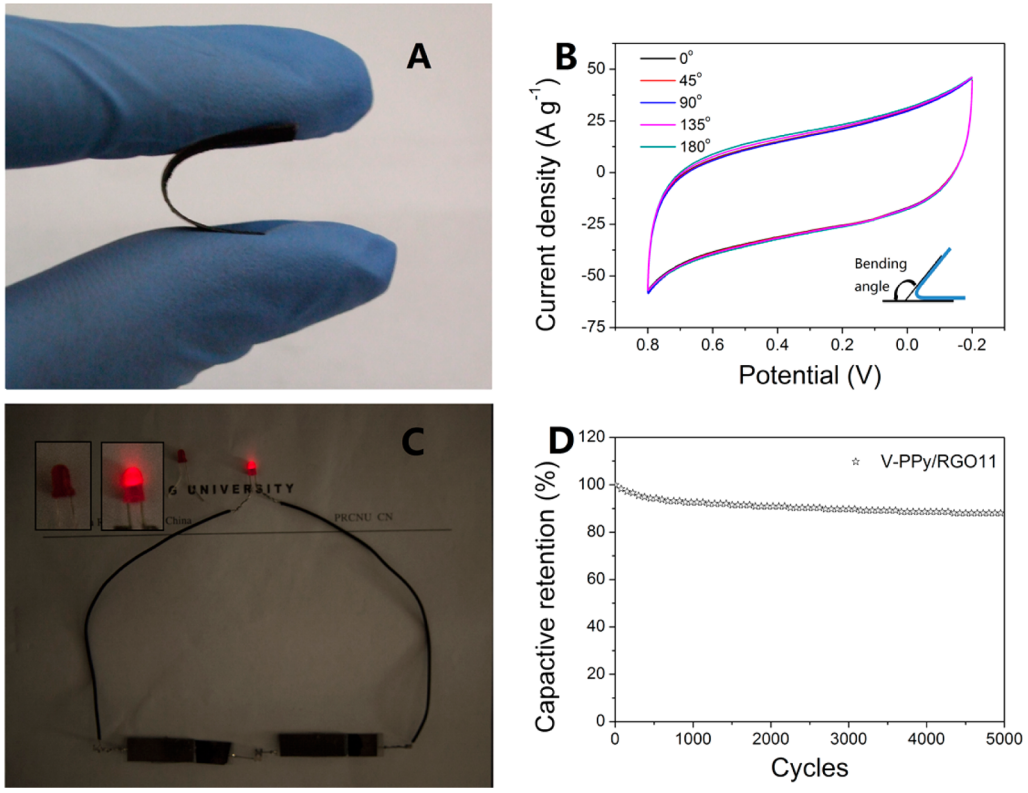

Figure 7. (A) Digital photograph of a flexible V-PPy/RGO thin film electrode. (B) CVs of the V-PPy/RGO11 all-solid-state flexible supercapacitor at 100 mV/s under different bending angles. (C) Photograph of a red LED powered by the two V-PPy/RGO11 supercapacitors in series. (D) Cycling stability of V-PPy/RGO11 during the long-term charge−discharge process.

meter four-probe system. All electrochemical measurements were performed on a CHI660d (Shanghai CH Instrument Company, China). The effective surface area was tested with a conventional three-electrode system consisting of a GCE (diameter = 3 mm), a platinum wire, and a saturated calomel electrode as the working electrode, the reference electrode, and the counter electrode, respectively.

The specific capacitance (C) of the all-solid-state supercapacitor was calculated using the following equations

$$C = \frac{I \cdot \Delta t}{\Delta V \cdot m} \tag{2}$$

where I is the current; Δt is the discharge time; ΔV is the potential window; and m is the mass of active material.

The energy density (E) and power density (P) were calculated according to the following equation

$$E = \frac{1}{2} C \Delta V^2; \quad P = \frac{E}{\Delta t} \tag{3}$$

■ ASSOCIATED CONTENT

Supporting Information

Additional characterizations and electrochemical data as described in the article. This material is available free of charge via the Internet at http://pubs.acs.org.

■ AUTHOR INFORMATION

Corresponding Authors

* E-mail: shishanwu@nju.edu.cn (S.W.).
*E-mail: chem100@nju.edu.cn (Q.C.).

Author Contributions

The manuscript was written through contributions of all authors. All authors have given approval to the final version of the manuscript.

Notes

The authors declare no competing financial interest.

■ ACKNOWLEDGMENTS

This work was supported by the National Natural Science Foundation of China (Nos. 51272100 and 51273073) and the Foundation of Jiangsu Collaborative Innovation Center of Biomedical Functional Materials.

■ REFERENCES

(1) Zhang, L. L.; Zhao, X. S. Carbon-Based Materials as Supercapacitor Electrodes. *Chem. Soc. Rev.* **2009**, *38*, 2520−2531.
(2) Simon, P.; Gogotsi, Y. Materials for Electrochemical Capacitors. *Nat. Mater.* **2008**, *7*, 845−854.
(3) Yuan, L. Y.; Xiao, X.; Ding, T. P.; Zhong, J. W.; Zhang, X. H.; Shen, Y.; Hu, B.; Huang, Y. H.; Zhou, J.; Wang, Z. L. Paper-Based Supercapacitors for Self-Powered Nanosystems. *Angew. Chem., Int. Ed.* **2012**, *51*, 4934−4938.
(4) Liu, J. P.; Jiang, J.; Cheng, C. W.; Li, H. X.; Zhang, J. X.; Gong, H.; Fan, H. J. Co_3O_4 Nanowire@MnO_2 Ultrathin Nanosheet Core/Shell Arrays: A New Class of High-Performance Pseudocapacitive Materials. *Adv. Mater.* **2011**, *23*, 2076−2081.
(5) El-Kady, M. F.; Strong, V.; Dubin, S.; Kaner, R. B. Laser Scribing of High-Performance and Flexible Graphene-Based Electrochemical Capacitors. *Science* **2012**, *335*, 1326−1330.
(6) Kaempgen, M.; Chan, C. K.; Ma, J.; Cui, Y.; Gruner, G. Printable Thin Film Supercapacitors Using Single-Walled Carbon Nanotubes. *Nano Lett.* **2009**, *9*, 1872−1876.

(7) Zhang, C.; Yin, H.; Han, M.; Dai, Z.; Pang, H.; Zheng, Y.; Lan, Y.-Q.; Bao, J.; Zhu, J. Two-Dimensional Tin Selenide Nanostructures for Flexible All-Solid-State Supercapacitors. *ACS Nano* **2014**, *8*, 3761−3770.
(8) Lu, X.; Yu, M.; Wang, G.; Zhai, T.; Xie, S.; Ling, Y.; Tong, Y.; Li, Y. H-TiO_2@ MnO_2//H-TiO_2@C Core-Shell Nanowires for High Performance and Flexible Asymmetric Supercapacitors. *Adv. Mater.* **2013**, *25*, 267−272.
(9) Liu, M.; Miao, Y. E.; Zhang, C.; Tjiu, W. W.; Yang, Z.; Peng, H.; Liu, T. Hierarchical Composites of Polyaniline-Graphene Nanoribbons-Carbon Nanotubes as Electrode Materials in All-Solid-State Supercapacitors. *Nanoscale* **2013**, *5*, 7312−7320.
(10) Meng, Y.; Zhao, Y.; Hu, C.; Cheng, H.; Hu, Y.; Zhang, Z.; Shi, G.; Qu, L. All-Graphene Core-Sheath Microfibers for All-Solid-State, Stretchable Fibriform Supercapacitors and Wearable Electronic Textiles. *Adv. Mater.* **2013**, *25*, 2326−2331.
(11) Yang, X.; Zhang, L.; Zhang, F.; Zhang, T.; Huang, Y.; Chen, Y. A high-performance all-solid-state supercapacitor with graphene-doped carbon material electrodes and a graphene oxide-doped ion gel electrolyte. *Carbon* **2014**, *72*, 381−386.
(12) Yang, C.; Shen, J.; Wang, C.; Fei, H.; Bao, H.; Wang, G. All-Solid-State Asymmetric Supercapacitor Based on Reduced Graphene Oxide/Carbon Nanotube and Carbon Fiber Paper/Polypyrrole Electrodes. *J. Mater. Chem. A* **2014**, *2*, 1458−1464.
(13) Peng, L.; Peng, X.; Liu, B.; Wu, C.; Xie, Y.; Yu, G. Ultrathin Two-Dimensional MnO_2/Graphene Hybrid Nanostructures for High-Performance, Flexible Planar Supercapacitors. *Nano Lett.* **2013**, *13*, 2151−2157.
(14) Yang, P.; Ding, Y.; Lin, Z.; Chen, Z.; Li, Y.; Qiang, P.; Ebrahimi, M.; Mai, W.; Wong, C. P.; Wang, Z. L. Low-Cost High-Performance Solid-State Asymmetric Supercapacitors Based on MnO_2 Nanowires and Fe_2O_3 Nanotubes. *Nano Lett.* **2014**, *14*, 731−736.
(15) Zhou, W.; Liu, X.; Sang, Y.; Zhao, Z.; Zhou, K.; Liu, H.; Chen, S. Enhanced Performance of Layered Titanate Nanowire-Based Supercapacitor Electrodes by Nickel Ion Exchange. *ACS Appl. Mater. Interfaces* **2014**, *6*, 4578−4586.
(16) Yuan, L.; Yao, B.; Hu, B.; Huo, K.; Chen, W.; Zhou, J. Polypyrrole-Coated Paper for Flexible Solid-State Energy Storage. *Energy Environ. Sci.* **2013**, *6*, 470−476.
(17) Sellam; Hashmi, S. A. High Rate Performance of Flexible Pseudocapacitors fabricated using Ionic-Liquid-Based Proton Conducting Polymer Electrolyte with Poly(3,4-ethylenedioxythiophene): Poly(styrene sulfonate) and Its Hydrous Ruthenium Oxide Composite Electrodes. *ACS Appl. Mater. Interfaces* **2013**, *5*, 3875−3883.
(18) Geim, A. K.; Novoselov, K. S. The rise of grapheme. *Nat. Mater.* **2007**, *6*, 183−191.
(19) Sun, Y.; Wu, Q.; Shi, G. Graphene Based New Energy Materials. *Energy Environ. Sci.* **2011**, *4*, 1113−1132.
(20) Pei, S. F.; Cheng, H. M. The Reduction of Graphene Oxide. *Carbon* **2012**, *50*, 3210−3228.
(21) Meng, Y.; Wang, K.; Zhang, Y.; Wei, Z. Hierarchical Porous Graphene/Polyaniline Composite Film with Superior Rate Performance for Flexible Supercapacitors. *Adv. Mater.* **2013**, *25*, 6985−6990.
(22) Lei, Z.; Shi, F.; Lu, L. Incorporation of MnO_2-Coated Carbon Nanotubes between Graphene Sheets as Supercapacitor Electrode. *ACS Appl. Mater. Interfaces* **2012**, *4*, 1058−1064.
(23) Zhang, Z.; Xiao, F.; Guo, Y.; Wang, S.; Liu, Y. One-Pot Self-Assembled Three-Dimensional TiO2-Graphene Hydrogel with Improved Adsorption Capacities and Photocatalytic and Electrochemical Activities. *ACS Appl. Mater. Interfaces* **2013**, *5*, 2227−2233.
(24) Zhang, Z.; Xiao, F.; Qian, L.; Xiao, J.; Wang, S.; Liu, Y. Facile Synthesis of 3D MnO_2-Graphene and Carbon Nanotube−Graphene Composite Networks for High-Performance, Flexible, All-Solid-State Asymmetric Supercapacitors. *Adv. Energy Mater.* **2014**, DOI: 10.1002/aenm.201400064.
(25) Lu, L.; Liu, J.; Hu, Y.; Zhang, Y.; Randriamahazaka, H.; Chen, W. Highly Stable Air Working Bimorph Actuator Based on A Graphene Nanosheet/Carbon Nanotube Hybrid Electrode. *Adv. Mater.* **2012**, *24*, 4317−4321.
(26) Deng, L.; Hao, Z.; Wang, J.; Zhu, G.; Kang, L.; Liu, Z. H.; Yang, Z.; Wang, Z. Preparation and Capacitance of Graphene/Multiwall Carbon Nanotubes/MnO_2 Hybrid Material for High-Performance Asymmetrical Electrochemical Capacitor. *Electrochim. Acta* **2013**, *89*, 191−198.
(27) Zhang, J.; Yu, Y.; Liu, L.; Wu, Y. Graphene-Hollow PPy Sphere 3D-Nanoarchitecture with Enhanced Electrochemical Performance. *Nanoscale* **2013**, *5*, 3052−3057.
(28) Qian, T.; Yu, C.; Wu, S.; Shen, J. A Facilely Prepared Polypyrrole−Reduced Graphene Oxide Composite with A Crumpled Surface for High Performance Supercapacitor Electrodes. *J. Mater. Chem. A* **2013**, *1*, 6539−6542.
(29) Chi, K.; Zhang, Z.; Xi, J.; Huang, Y.; Xiao, F.; Wang, S.; Liu, Y. Freestanding Graphene Paper Supported Three-Dimensional Porous Graphene− Polyaniline Nanocomposite Synthesized by Inkjet Printing and in Flexible All-Solid-State Supercapacitor. *ACS Appl. Mater. Interfaces* **2014**, DOI: 10.1021/am504539k.
(30) Liu, A. R.; Li, C.; Bai, H.; Shi, G. Q. Electrochemical Deposition of Polypyrrole/Sulfonated Graphene Composite Films. *J. Phys. Chem. C* **2010**, *114*, 22783−22789.
(31) Zhang, Z.; Yuan, Y.; Liang, L.; Cheng, Y.; Xu, H.; Shi, G.; Jin, L. Preparation and Photoelectrochemical Properties of A Hybrid Electrode Composed of Polypyrrole Encapsulated in Highly Ordered Titanium Dioxide Nanotube Array. *Thin Solid Films* **2008**, *516*, 8663−8667.
(32) Zhang, J.; Chen, P.; Oh, B. H. L.; Chan-Park, M. B. High Capacitive Performance of Flexible and Binder-Free Graphene−Polypyrrole Composite Membrane Based on In Situ Reduction of Graphene Oxide and Self-Assembly. *Nanoscale* **2013**, *5*, 9860−9866.
(33) Wang, G. P.; Zhang, L.; Zhang, J. J. A Review of Electrode Materials for Electrochemical Supercapacitors. *Chem. Soc. Rev.* **2012**, *41*, 797−828.
(34) Wu, T. M.; Chang, H. L.; Lin, Y. W. Synthesis and Characterization of Conductive Polypyrrole/Multi-Walled Carbon Nanotubes Composites with Improved Solubility and Conductivity. *Compos. Sci. Technol.* **2009**, *69*, 639−644.
(35) Fan, J.; Wan, M.; Zhu, D.; Chang, B.; Pan, Z.; Xie, S. Synthesis, Characterizations, and Physical Properties of Carbon Nanotubes Coated by Conducting Polypyrrole. *J. Appl. Polym. Sci.* **1999**, *74*, 2605−2610.
(36) Huang, Y. J.; Qin, Y. W.; Zhou, Y.; Niu, H.; Yu, Z. Z.; Dong, J. Y. Polypropylene/Graphene Oxide Nanocomposites Prepared by In Situ Ziegler-Natta Polymerization. *Chem. Mater.* **2010**, *22*, 4096−4102.
(37) Ibris, N.; Salvi, A. M.; Liberatore, M.; Decker, F.; Surca, A. XPS Study of The Li Intercalation Process in Sol-Gel-Produced V_2O_5 Thin Film: Influence of Substrate and Film Synthesis Modification. *Surf. Interface Anal.* **2005**, *37*, 1092−1104.
(38) Zhao, X.; Zhang, Q. H.; Chen, D. J.; Lu, P. Enhanced Mechanical Properties of Graphene-Based Poly(vinyl alcohol) Composites. *Macromolecules* **2010**, *43*, 2357−2363.
(39) Jiang, H.; Wang, X. M. Highly Sensitive Detection of Daunorubicin Based on Carbon Nanotubes−Drug Supramolecular Interaction. *Electrochem. Commun.* **2009**, *11*, 126−129.
(40) Li, S.; Zhao, C.; Shu, K.; Wang, C.; Guo, Z. P.; Wallace, G. G.; Liu, H. Mechanically Strong High Performance Layered Polypyrrole Nano Fibre/Graphene Film for Flexible Solid State Supercapacitor. *Carbon* **2014**, *79*, 554−562.
(41) Zhao, C.; Wang, C.; Yue, Z.; Shu, K.; Wallace, G. G. Intrinsically Stretchable Supercapacitors Composed of Polypyrrole Electrodes and Highly Stretchable Gel Electrolyte. *ACS Appl. Mater. Interfaces* **2013**, *5*, 9008−9014.
(42) Bailey, J. K.; Pozarnsky, G. A.; Mecartney, M. L. The Direct Observation of Structural Development During Vanadium Pentoxide Gelation. *J. Mater. Res.* **1992**, *7*, 2530−2537.
(43) Hummers, W. S.; Offeman, R. E. Preparation of Graphitic Oxide. *J. Am. Chem. Soc.* **1958**, *80*, 1339−1339.